https://doi.org/10.5194/acp-2021-147
Preprint. Discussion started: 7 April 2021

Atmospheric Chemistry and Physics
Discussions
Open Access

Roles of the Inner Eyewall Structure in the Secondary Eyewall Formation of Simulated Tropical Cyclones

Nannan Qin[1,2], Liguang Wu[1,4], Qingyuan Liu[3]

[1]Department of Atmospheric and Oceanic Sciences and Institute of Atmospheric Sciences, Fudan University, Shanghai, 200438, China

[2]State Key Laboratory of Severe Weather, Chinese Academy of Meteorological Sciences, Beijing, 100081, China

[3]Nanjing Joint Institute for Atmospheric Sciences, Nanjing, China
[4]Innovation Center of Ocean and Atmosphere System, Zhuhai Fudan Innovation Research Institute，Zhuhai, 518057, China

Correspondence to: Dr. Liguang Wu (liguangwu@fudan.edu.cn)

https://doi.org/10.5194/acp-2021-147
Preprint. Discussion started: 7 April 2021

Abstract. It has been suggested that the inner eyewall structure may play an important role in the secondary eyewall formation (SEF) of tropical cyclones (TCs). This study is to further examine the role of the inner eyewall structure by comparing two numerical experiments, which were conducted with the same large-scale environment and initial and boundary conditions but different grid sizes. The SEF was simulated in the experiment with the finer grid spacing, but not in the other.

Comparing the eyewall structure in the simulated TCs with and without the SEF indicates that the eyewall structure can play an important role in the SEF. For the simulated TC with the SEF, the eyewall is more upright with stronger updrafts, accompanied by a wide eyewall anvil at a higher altitude. Compared to the simulated TC without the SEF, diagnostic analysis reveals that the cooling outside the inner eyewall is induced by the sublimation, melting and evaporation of hydrometeors falling from the eyewall anvil. The cooling also induces upper-level dry, cool inflow below the anvil, prompting the subsidence and moat formation between the inner eyewall and the spiral rainband. In the simulated TC without the SEF, the cooling induced by the falling hydrometeors is significantly reduced and offset by the diabatic warming. There is no upper-level dry inflow below the anvil and no moat formation between the inner eyewall and the spiral rainband. This study suggests that a realistic simulation of the intense eyewall convection is important to the prediction of the SEF in the numerical forecasting model.

1 Introduction

Many intense tropical cyclones (TCs) usually undergo the secondary eyewall formation (SEF) (Fortner, 1958; Willoughby, 1982). Observational study shows that about 80% of intense TCs (maximum surface wind > 62 m s^{-1}) in the western North Pacific, 70% in the Atlantic, and 50% in the eastern Pacific possessed concentric eyewalls at least once (Hawkins and Helveston, 2008). The eyewall replacement circle is one of the most important issues remaining in understanding and predicting the change of TC intensity due to the resulting dramatic intensity fluctuations (Samsury and Zipser, 1995; Terwey and Montgomery, 2008; Bell et al., 2012). Although much effort has been made to understand the mechanisms of the SEF, a consensus has not been reached so far.

Previous studies have pointed out the dynamic importance of the vortex circulation in the SEF (Montgomery and Kallenbach, 1997; Chen and Yau, 2001; Qiu et al., 2010). Given a negative radial gradient of vorticity outside the primary eyewall, vortex Rossby waves (VRWs) propagate outward and stop at a stagnation radius, where the mean flow strengthens through the interaction of eddies with the azimuthal-mean vortex (Montgomery and Kallenbach, 1997; Qiu et al., 2010; Chen and Yau, 2001; Hogsett and Zhang, 2009; Dai et al., 2021). With the strengthening mean flow, the outer convection occurs and evolves into an outer eyewall through the wind-induced surface heat exchange (Emanuel, 1986). Terwey and Montgomery (2008) proposed that cumulus convection forms and maintains in a far-field region with a weak negative radial gradient of vorticity (the β–skirt) and moderate stretching time. A secondary eyewall forms through the upscale cascade and axisymmetrization of eddy vorticities in the sustained convection. It has been found that the secondary eyewall can be simulated in a barotropic model when the preexisting outer convection is stretched into a closed vorticity band by the rotation of the inner vortex (Kuo et al., 2004, 2008). Based on a nonlinear boundary layer model, Kepert (2013) proposed that the secondary eyewall can form through a positive feedback among the local enhancement of the radial vorticity gradient, the frictional updraft. Those studies highlight the positive feedback of the eddy kinetic energy to the storm-scale flow through the dynamics of the VRW, vorticity interaction, and the Ekman pumping. However, the convective activity related to the generation of the eddy kinetic energy is not fully addressed.

Some studies focused on spiral rainbands because the SEF generally starts from convective rainbands (Houze, 2007; Zhao et al., 2008, 2016; Kossin and Sitkowski, 2009). When the rainband outside the eyewall is enhanced by adding a large diabatic heating rate to the rainband in a numerical simulation, the TC can experience the SEF (Wang, 2009). Zhu and Zhu (2014) emphasized that a critical strength of the rainbands is needed for the formation of a secondary wind maximum through diabatic heating. Idealized numerical simulations indicated that the sustained convection in the SEF region was enhanced by the interaction between the unbalanced boundary layer process and the asymmetric inflows induced by the outside rainbands that propagated inward (Qiu and Tan, 2013; Wang and Tan, 2020). Recent studies revealed that, for SEF cases, the descending inflow in the downwind portion of the spiral rainbands transfers high angular momentum inward, leading to the outward expansion of the wind field (Didlake et al., 2018; Wunsch and Didlake, 2018; Wang et al., 2019; Yu et al., 2020). A radial expansion of storm wind precedes the SEF through the boundary layer processes and coupled convective dynamics (Rozoff et al., 2012; Huang et al., 2012; Abarca and Montgomery, 2013; Sun et al., 2013). However, not all the spiral rainbands outside of the TC eyewall can evolve into a closed outer eyewall.

Many numerical studies have also shown the importance of various microphysical processes in the SEF since the inner-core structure and intensity of TCs are sensitive to the microphysical processes (Wang, 2002; Zhu and Zhang, 2006). Zhu and Zhang (2006) proposed that varying cloud microphysics processes affect the timing of the spinup of the secondary eyewall since the differences in the inner eyewall convection and the rainband structure of the simulated TCs. Numerical simulations showed that changing the terminal velocity of snow led to changes in the magnitude and distribution of the diabatic heating of inner-core convection at outer radii, which is important for the SEF (Zhu and Zhu, 2015). Influenced by the evaporative cooling from the fallout of hydrometeors, the penetrative downdrafts can promote the local convection outside the primary eyewall, where the SEF occurs (Tyner et al., 2018). Moreover, microphysical processes are also important to the occurrence of the moat, by which the spiral rainband is separated from the inner eyewall with a chance to become a secondary eyewall. Willoughby et al. (1982) considered the moat generated with subsidence as the evaporative cooling of precipitation falling from the cumulus anvil. In our previous study based on a numerical modeling simulation (Qin et al., 2021), we demonstrated that the moat subsidence is mainly caused by the negative buoyancy resulting from the cooling from sublimation, melting and evaporation processes of hydrometeors from the cumulus eyewall and the related well-developed anvil, and the moat subsidence is further enhanced by the compensating upper-level dry-air inflows.

The objective of this study is to further examine the roles of the inner eyewall structure and the associated cooling in the formation of the moat between the inner eyewall and the spiral rainband that later becomes the outer eyewall. Our examination was based on two numerical experiments with the same large-scale environment and initial and boundary conditions, but different grid sizes since the strength and distribution of the inner-core convection of TCs are sensitive to the horizontal resolutions (Zhang et al., 2015; Qin and Zhang, 2018; Wu et al., 2018, 2019). This paper is organized as follows. Section 2 briefly summarizes the experimental design.

https://doi.org/10.5194/acp-2021-147
Preprint. Discussion started: 7 April 2021

Section 3 describes the simulated TCs with different horizontal spacings. In Section 4, different eyewall structures are identified, followed by Section 5, in which how the differences in the eyewall structure affect the SEF is investigated. A summary and concluding remarks are given in the final section.

2 Experimental design

In our previous study, a 72-h simulation (CTL) was conducted using the Weather Research and Forecasting model (WRF, version 3.2.1) with quintuply nested domains (27/9/3/1/0.3 km), in which the simulated TC experienced the SEF (Qin et al., 2021). In order to understand the influence of structural changes of the eyewall on the SEF, a sensitivity experiment (NSEF) was further designed by removing the innermost domain used in CTL. The two experiments were conducted over the open ocean for 72 hours. The sea surface temperature is fixed at 29 ℃. The outermost domain is centered at 30 °N, 132.5 °E. The domains with the grid spacing of 3 km and less moved with the TC center. There are 75 vertical levels with the model top at 50 hPa. The National Centers for Environmental Prediction (NCEP) Final Operational Global Analysis data (1° ×1°) is utilized for the initial and lateral boundary conditions. The simulations begin with a TC-like vortex.

Model physics options are the same as those used in Chen and Wu (2016) and Qin et al. (2021). The major model physics options include the single-moment 3-class microphysics scheme for the outermost domain, the single-moment 6-class microphysics scheme for the rest of the domains, the Yonsei University planetary boundary layer (PBL) scheme (Noh et al., 2003), the longwave radiation scheme of the Rapid Radiative Transfer Model (RRTM, Mlawer et al., 1997), the shortwave radiation scheme of the Dudhia (Dudhia, 1989). The Kain-Fritsch cumulus parameterization scheme (Kain and Fritsch, 1993) is applied only in the outermost domain.

3 Evolution of the simulated TCs

There is little difference in the track of the simulated storms largely because the large-scale environmental conditions are the same in the two experiments (figure not shown). Despite the same large-scale environment and initial and boundary conditions, the intensity evolution is different in the two simulations (Fig. 1). In NSEF, after an 18-h spin-up, the near-surface maximum wind speed (V_{MAX}) experiences a persistent increase and reaches its peak intensity of 62.5 m s^{-1} at 57 h, then the V_{MAX} decreases. In CTL, the storm experiences a weakening stage from 32 h to 48 h and a reintensification from 48 h to 63 h due to the SEF. There are pronounced fluctuations in the V_{MAX} in CTL, suggesting the influence of the small-scale structures simulated with the finer grid size in the innermost domain.

The different eyewall structures between the two experiments can be seen from the evolution of the azimuthal-mean tangential wind. Figure 2 compares the time-radius cross-sections of the azimuthal-mean tangential wind and the vertical motion at 0.5 km between the two simulations. In NSEF, a single maximum wind core maintains and the tangential wind expands radially outward during the intensification. It is indicated that no SEF occurs in this experiment. In CTL, the simulated TC experiences the SEF, as discussed in Qin et al. (2021). The formation of the secondary eyewall begins around 32 h with a secondary maximum tangential wind of over 35 m s^{-1} at the radius of 85 km. After the SEF, the outer eyewall contracts and intensifies with its strength catching up with the primary eyewall at t = 40 h (Fig. 2b). A few hours later, the primary eyewall weakens and is replaced by the new eyewall around 46 h.

The different inner-core structures can also be seen in the evolution of the azimuthal-mean vertical motion (Figs. 2c and 2d). In NSEF, the strong upward motion in the single eyewall is maintained during the 72-h simulation. The vertical motion in the eyewall with a speed larger than

0.2 m s^{-1} extends about 20-30 km at 0.5-km height. In CTL, prior to the SEF, the primary eyewall contracts inward and the width of the eyewall with the upward motion over 0.2 m s^{-1} is reduced. Around 34 h, a secondary maximum upward motion occurs at a radius of around 60 km. After the SEF, the weakening and dissipation of the primary eyewall can also be seen from the upward motion shown in Fig. 2d. It is seen that the double eyewall structure exists for 14 h.

Moreover, the simulated inner rainbands evolve differently in the two experiments. Figure 3 shows the horizontal distributions of the 5-km radar reflectivity at the selected times. In NSEF, the broad and active rainband is evident in the downshear quadrant of the storm, while the rainband in the upshear quadrant is weak with sporadic convection located around the radii of 100-150 km at 28 h. Afterward, the rainbands contract and merge with the inner eyewall, leading to an expansion of the wind field and a broad single eyewall without the formation of a moat. In CTL, the rainbands show a pattern similar to that in NSEF by 28 h (Fig. 3d), but the rainbands are elongated azimuthally and became a closed ring outside the primary eyewall by 32 h. A clear moat region forms at 50-60 km radii between the primary and the outer eyewalls. After a weakening stage, the primary eyewall almost dissipates by 44 h (Fig. 3f), followed by an inward contraction of the outer eyewall.

4 Differences in the vertical structures of the eyewall

One of the major differences in the eyewall between NSEF and CTL is the magnitude and the vertical distribution of the vertical motion, which can be examined with the azimuthally averaged vertical motion within the radius of 100 km (Fig. 4) and the contoured frequency by altitude diagram (CFAD) of the vertical motion (Fig. 5a). The CFAD illustrates the frequency distribution of the vertical motion of the indicated values at each altitude in the region of the 10-km radially inside and outside of the radius of the maximum tangential wind (RMW) for two simulations. The azimuthal-mean upward motion in the eyewall is stronger in CTL than that in NSEF (Fig. 4). Specifically, the upward motion in the eyewall in NSEF is maximized at 10- and 12-km height with peaks of 11 and 13 m s^{-1} for the 0.1 % and 0.05% percentiles (Fig. 5a), respectively. The weak upward motion between 45- to 75-km radii is associated with the broad rainbands (Figs. 4a and 4b). In contrast, the maximum upward motion in CTL is 12 and 14 m s^{-1} for the 0.1 % and 0.05% percentiles (Fig. 5a). The stronger upward motion in CTL indicates that a higher resolution in the model simulation can resolve more intense eyewall updrafts (Yau et al., 2004). Moreover, the eyewall with strong updrafts in CTL is more upright in the vertical direction.

Another important difference in the eyewall between NSEF and CTL is the feature of the upper-level outflow layer. Figure 5b compares the upper-level outflow in the two simulations by showing the 0.1% and 0.05% contoured frequency of the radial wind in the region of a radial distance of 60 km starting from the radius of 10-km outside the eyewall. In NSEF, the upper-level outflow peaks around the 11-km height with maxima of 28 and 26 m s^{-1} for the 0.05% and 0.1% percentages, respectively. The outflow layer is deep with a magnitude of over 15 m s^{-1} extending downward to 8 km. In CTL, the maximum outflow with values of over 29 m s^{-1} is located around the 14-km height. The outflow layer at the higher altitude in CTL is associated with the strong upward motion in the eyewall that can lift the hydrometeors much higher.

The different eyewall structures can also be seen in the horizontal distribution of the cloud-top temperature (Fig. 6). In NSEF, the eyewall is wider and possesses relatively weaker convection as indicated by the cloud-top temperature of above -75^{0}C (Fig. 6a). In CTL, the cloud associated with the eyewall is deeper since the coldest cloud-top temperature is below -75 ^{0}C (Fig. 6b). The coldest cloud-top temperature is located at the downshear- and upshear-right region due to the influence of the southeastward VWS. The strong eyewall convection is accompanied by the strong and high-altitude outflow compared to that in NSEF.

5 Influence of the eyewall structure on the moat formation

5.1 Buoyancy effects

As discussed above, the rainbands can encircle into a closed outer eyewall instead of merging with the inner eyewall in CTL due to the formation of the moat. First, we investigate the relationship between the distribution of buoyancy and the occurrence of the moat subsidence. Many studies indicated that buoyance, which is determined by temperature perturbation, affects the vertical motion tendency (e.g., Zhang et al., 2000; Braun, 2002; Miller et al., 2015). It is intended to examine how the buoyancy changes when the SEF fails in NSEF with a different eyewall structure. Following the method used by Braun (2002), the perturbation associated with the buoyance calculation is defined as $A'(\lambda, r, z) = A(\lambda, r, z) - A_0(z) - A^{0,1}(\lambda, r, z)$, where A represents any variable in a cylindrical coordinate (λ, r, z), λ, r, z are the azimuthal angle, the radius from the TC center, and the vertical height axis, respectively, A_0 is averaged over the whole area of the 1-km domain, $A^{0,1}$ are the wavenumber-0 and -1 components of the perturbation field from A_0. $A_0 + A^{0,1}$ denotes the reference state for the buoyance analysis. Following Houze (1993) and Braun (2002), buoyancy (B) is defined as:

$$B = g\left[\frac{\theta_v'}{\theta_{v0}+\theta_v^{0,1}} + (\kappa - 1)\frac{p'}{p_0+p^{0,1}} - q'\right], \tag{1}$$

where g is the gravitational acceleration, θ_v is the virtual potential temperature, $\kappa = 0.286$, p is the pressure, and q is the hydrometeor mixing ratio, including the mixing ratio of the cloud water (q_c), rain water (q_r), graupel (q_g), snow (q_s), and ice (q_i). Terms on the right-hand side of Eq. (1) are the thermal buoyancy, the dynamic buoyancy, and the hydrometeor loading, respectively. Considering that the rainband distributes asymmetrically prior to the SEF, it is appropriate to use quarter-mean variables, i.e. the upshear-right quadrant, to analyze the moat and outer eyewall formation in our following discussions.

For the convenience of the following buoyancy analysis, Fig. 7 shows the radius-height cross sections of the perturbation virtual potential temperature (θ_v'). Consistent with the broad eyewall convection in NSEF, positive θ_v' appears under the eyewall anvil, which may force the air parcel upward since the local θ_v exceeds the ambient environmental value. On the contrary, the θ_v' is negative outside and underneath the inner eyewall in CTL (Fig. 7e), which will suppress the upward motion there.

Given the different distribution of θ_v', we next examine the related thermal buoyancy, as well as the dynamic buoyancy and the hydrometeor loading (Fig. 8). In NSEF, we note that the positive buoyancy coinciding with the positive θ_v' appears outside the inner eyewall since the buoyancy is largely determined by the thermal buoyancy and the dynamical buoyancy and the water loading effects are relatively small (Figs. 8a-8d). The positive buoyancy forces upward motion, leading to the widespread upward motion in NSEF (Fig. 8b). There is no moat formation without the considerable subsidence, and the spiral rainband merges with the primary eyewall and no SEF occurs. In CTL, the emergence of the moat subsidence is largely caused by the negative buoyancy, especially the negative thermal buoyancy in response to the negative θ_v' outside the inner eyewall. Moreover, the dynamic buoyancy and the water loading effect both contribute to the enhancement of the moat subsidence. Note that the negative buoyancy also occurs in the inner eyewall below 6-km height (Fig. 8e), which is consistent with the weakening of the primary eyewall when the outer eyewall intensifies. These results indicate that the negative buoyancy beneath the high-altitude eyewall anvil from the inner eyewall is crucial for the subsidence generation and the moat emergence. The moat plays an important role in the SEF by separating the preexisting spiral rainbands from the inner eyewall.

https://doi.org/10.5194/acp-2021-147
Preprint. Discussion started: 7 April 2021

To further demonstrate the tendency of the vertical motion, the perturbation vertical pressure gradient force and the net force among the buoyancy and the perturbation vertical pressure gradient force are shown in Fig. 9. Even though the perturbation vertical pressure gradient force exhibits oppositely to the buoyancy in the two simulated TCs, the net force contributes to the upward acceleration of updrafts in NSEF (Fig. 9c) but the downward acceleration of the subsidence outside the primary eyewall in CTL (Fig. 9f). As a result, the subsidence outside the inner eyewall in CTL contributes to the formation of the moat, followed by the SEF, while no SEF occurs in NSEF without the emergence of the moat.

5.2 Diabatic heating

Since the negative buoyancy is associated with the negative temperature disturbance, the diabatic heating is examined. Figure 10 shows the radius-height distributions of the diabatic heating and diabatic cooling induced by the sublimation, melting, and evaporation of hydrometeors. In NSEF, the diabatic warming dominates the region within the radius of 100 km, except for the eye and a local area around 40-km radius from 1- to 6-km heights (Fig. 10a). This broad warming is caused by the wider eyewall convection as shown in Fig. 3 and Fig 4a. Although the diabatic cooling related to the sublimation, melting and evaporation processes always exist in the storm (Figs. 10b-10d), the low- to middle-level convection outside the inner eyewall produces much diabatic warming than cooling, leading to net diabatic warming appearing outside the primary eyewall in NSEF. In contrast, instead of diabatic warming, the net diabatic cooling appears with the absence of convection outside of the inner eyewall in CTL (Fig. 10e). This cooling is maximized at 6- to 10-km height, which is largely induced by the sublimation of hydrometeors beneath the eyewall anvil (Figs. 10f-10h), while the cooling located below 6-km height is caused by the melting and evaporative processes.

https://doi.org/10.5194/acp-2021-147
Preprint. Discussion started: 7 April 2021

The evolution of subsidence in the moat area is largely controlled by the distribution of the diabatic cooling. The azimuthal extension of the diabatic cooling and the related moat subsidence and their differences in CTL and NSEF at upper levels are further examined in Fig. 11. Before 24 h, both the diabatic cooling and the related subsidence in NSEF and CTL are characterized by a highly asymmetric structure with intense subsidence/cooling located in the upshear-left quadrant (see Figs. 11a, 11b, and Fig. 3). After 24 h, the evolution of the diabatic cooling and subsidence differs in the two simulations. The asymmetric structure of the intense diabatic cooling and subsidence maintains in NSEF, while the diabatic cooling and subsidence extend cyclonically from the upshear-left quadrant to the downshear-right quadrant, ending with a quasi-symmetric structure from 24 h to 32 h (Fig. 11b), which is also confirmed by showing the differences in the diabatic cooling and moat subsidence between NSEF and CTL in Fig. 11c.

5.3 Subsidence in response to the diabatic cooing

The Sawyer-Eliassen equation (SEE) is used to better understand how the diabatic heating with the different eyewall structures affects the evolution of the moat and outer eyewall without considering the momentum forcing. The SEE is a useful analytical tool for diagnosing the response of the transverse circulation to diabatic heating (Smith et al., 2005; Bui et al., 2009; Zhu and Zhu, 2014; Qin et al., 2021). According to Qin et al. (2021), the SEE used in this study is

$$\frac{\partial}{\partial r}\left[\frac{\chi}{\rho r}\frac{\partial b}{\partial z}\frac{\partial \psi}{\partial r}-\frac{\chi}{\rho r}\frac{\partial b}{\partial r}\frac{\partial \psi}{\partial z}\right]+\frac{\partial}{\partial z}\left[\left(\chi\xi\zeta_a-\frac{C\chi}{g}\frac{\partial b}{\partial r}\right)\frac{1}{\rho r}\frac{\partial \psi}{\partial z}-\frac{\chi}{\rho r}\frac{\partial b}{\partial r}\frac{\partial \psi}{\partial r}\right]=g\frac{\partial \chi^2 Q}{\partial r}+\frac{\partial C\chi^2 Q}{\partial z}, \tag{2}$$

where $\chi = 1/\theta$ and θ is the potential temperature, ρ is the density, b is the buoyancy term, ψ is a stream function, $\xi = 2v/r + f$ is the local Coriolis parameter and f is the Coriolis parameter, ζ_a is the vertical component of the absolute vorticity, $C = v^2/r + fv$ is the sum of the centrifugal force and Coriolis force where v is the tangential wind, g is the gravitational acceleration, r and z are the radial and vertical coordinate, and Q is the diabatic heating rate (heating forcing). Note that,

https://doi.org/10.5194/acp-2021-147
Preprint. Discussion started: 7 April 2021

in the absence of the momentum forcing, the diagnosed radial inflow within the boundary layer is largely underestimated, while the diagnosed secondary circulation above the boundary is comparable to the simulated results, which is also found in other studies (Bui et al., 2009; Zhu and Zhu, 2014; Qin et al., 2021).

Figure 12 shows the radius-height cross sections of the SEE-diagnosed vertical and radial wind forced by the diabatic heating, diabatic cooling, and cooling induced by the sublimation, melting and evaporation of hydrometeors, respectively. Significantly, in NSEF, the diabatic heating released by the wider eyewall convection induces the upward motion and deep-layer outflows outside the inner eyewall, and a compensated downdraft in the eye (Fig. 12a). In CTL, intense diabatic cooling forces subsidence of over -0.3 m s^{-1} outside the inner eyewall, which contributes to the formation of the moat. Meanwhile, the diabatic cooling also induces the upper-level inflow below the strong outflow layer (Fig. 12e). These results suggest that the formation of the moat is sensitive to the diabatic heating, especially the diabatic cooling beneath the eyewall anvil.

Although the diabatic cooling caused by phase changes usually occurs in TCs, the magnitude of the diabatic cooling, especially the cooling due to the sublimation of ice particles, matters much in the formation of the moat (Figs. 12c and 12g). The cooling due to the sublimation process is much less outside the primary eyewall in NSEF compared to that in CTL (cf. Figs. 12c and 12g). In NSEF, the diabatic warming released by the low- to middle-level convection outside the primary eyewall exceeds the cooling, resulting in net diabatic warming (Fig. 12a). Thus, a wider eyewall with warming-forced upward motion prevails due to the positive feedback among the diabatic heating and the convection (Fig. 12a). In addition, the warming-forced upward motion is accompanied by the deep-layer outflow (Fig. 13a), under which the low-level inflow appears below the 8-km height (Fig. 13a), which brings moist air enhancing the convection in NSEF. In

CTL, with the considerable cooling forced by the sublimation outside of the inner eyewall (Fig. 12g), the subsidence is induced outside the primary eyewall. Of importance is that the cooling-forced inflow is located at a higher level, which send dry air inward (Fig. 13b). The penetration of dry air through the upper-level inflow plays an important role in increasing the diabatic cooling that promotes the subsidence. The cooling-induced subsidence contributes significantly to the formation of the moat. Subsequently, the spiral rainband evolves into the separated outer eyewall in CTL with the formation of the moat.

The differences in the azimuthal distributions of the subsidence and the related upper-level radial inflow between NSEF and CTL are shown in Fig. 14. In NSEF, a highly asymmetric structure with strong subsidence located in the upshear-left quadrant persists during 18-32 hours (Fig. 14a). Although there is upper-level inflow appearing in the upshear-right region (Fig. 14a), it is largely offset by the strong upper-level outflow, leading to net outflow at upper levels as seen in Fig. 13a. In contrast, the subsidence in CTL extends azimuthally, ending with a quasi-symmetric structure from 18 h to 32 h (Fig. 14b). The azimuthal extension of the subsidence follows the appearance of the upper-level inflow, which advects dry air inward to enhance the cooling processes. Therefore, without the penetration of dry air by the upper-level descending inflow, the diabatic cooling and the cooling-forced subsidence beneath the eyewall anvil are limited, which are unfavorable for the moat formation outside the inner eyewall.

6 Summary

In this study, two numerical experiments are conducted with the same large-scale environment and initial and boundary conditions. The simulated inner eyewall structures are different due to different grid spacings used in the two experiments. The SEF occurs in CTL with a fine resolution of 333 m, while no SEF occurs in the other with a coarse resolution of 1 km.

https://doi.org/10.5194/acp-2021-147
Preprint. Discussion started: 7 April 2021

There are two major differences in the eyewall structure by comparing the simulated TCs with and without the SEF. For the simulated TC with the SEF, the eyewall updrafts are stronger and the eyewall is more upright. The eyewall anvil is located at a higher altitude together with the deep eyewall convection. As illustrated in Fig. 15, the upper-level dry-air inflow beneath the high-altitude anvil from the inner eyewall is important to the formation of the moat. Diagnostic analysis indicates that the dry inflow below the eyewall anvil is induced by the diabatic cooling released by the sublimation, melting and evaporation of hydrometeors falling from the eyewall anvil. With the penetration of dry air by the upper-level inflow, subsidence occurs, promoting the formation of the moat between the inner eyewall and the spiral rainband. Afterward, the SEF occurs by showing the double eyewall structure and the moat with subsidence. In the TC without the SEF, the eyewall updrafts are weak and tilt much outward, showing an eyewall anvil at the lower altitude. The cooling induced by the falling hydrometeors beneath the low-altitude eyewall anvil is significantly reduced and offset by the diabatic warming. As a result, no upper-level dry-air inflow occurs below the eyewall anvil, and no moat forms between the inner eyewall and the spiral rainband.

Our study highlights the importance of the inner eyewall structure in the moat formation through the cooling-induced upper-level inflow and subsidence beneath the eyewall anvil. While the subsidence induced by the evaporative cooling from the precipitation at the outer radii from the anvil is revealed by Tyner et al. (2018), who emphasized the role of the penetrative downdraft in promoting the local rainband convection and the subsequent outer eyewall formation, the cooling-induced upper-level dry-air inflow and its important role in the moat formation are not mentioned in their study. Recent studies indicated that a mesoscale descending inflow driven by the middle-level melting and evaporative cooling in the downwind portion of the rainband can

https://doi.org/10.5194/acp-2021-147
Preprint. Discussion started: 7 April 2021

trigger new convective updrafts that are important to the subsequent SEF (Didlake et al., 2018; Wunsch and Didlake, 2018; Yu et al., 2020). In addition to the mesoscale descending inflow at middle levels, the upper-level dry inflow also contributes to the SEF by forcing the moat formation. In this sense, both the inner-eyewall and the rainband structures are important to the SEF. In addition, our study suggests that a realistic simulation of the eyewall convection is important to the prediction of the SEF in the numerical forecasting model.

Data availability. The simulation data is archived at the High-Performance Computing Center of Nanjing University of Information Science and Technology and is available upon request.

Author contributions. LW designed research; NQ conceptualized the analysis and wrote the manuscript; LW provided scientific suggestions for the manuscript. QL carried out the simulations and modified the model code. All authors were involved in helpful discussions and contributions to the manuscript.

Competing interests. The authors declare that they have no conflict of interest.

Acknowledgments. This study was jointly supported by the National Natural Science Foundation of China (41730961, 41675009, 42075072, 41905001), the Postdoctoral Science Foundation of China (2019M661342), the Natural Science Foundation of Jiangsu Province (BK20201505), and the Open Research Program of the State Key Laboratory of Severe Weather (2019LASW-A02). We would like to acknowledge the use of computational resources for conducting the simulations at the High-Performance Computing Center of Nanjing University of Information Science and Technology.

References

Abarca, S. F. and Montgomery, M. T.: Essential dynamics of secondary eyewall formation, J. Atmos. Sci., 70, 3216-3230, doi: https://doi.org/10.1175/JAS-D-12-0318.1, 2013.

Bell, M. M., Montgomery, M. T., and Lee, W. C.: An axisymmetic view of concentric eyewall evolution in Hurricane Rita (2005), J. Atmos. Sci., 69, 2414-2432, doi: https://doi.org/10.1175/JAS-D-11-0167.1, 2012.

Braun, S. A.: A cloud-resolving simulation of Hurricane Bob (1991): Storm structure and eyewall buoyancy, Mon. Wea. Rev., 130, 1573-2432, doi: https://doi.org/10.1175/1520-0493(2002)130<1573:ACRSOH>2.0.CO;2, 2002.

Bui, H. H., Smith, R. K., Montgomery, M. T., and Peng, J.: Balanced and unbalanced aspects of tropical cyclone intensification, Q. J. R. Meteorol. Soc., 135, 1715-1731, doi: https://doi.org/10.1002/qj.502, 2009.

Chen, Y. and Yau, M. K.: Spiral bands in a simulated hurricane. Part I: Vortex Rossby wave verification, J. Atmos. Sci., 58, 2128-2145, doi: https://doi.org/10.1175/1520-0469(2001)058<2128:SBIASH>2.0.CO;2, 2001.

Chen X. and Wu, L.: Topographic influence on the motion of tropical cyclones landfalling on the coast of China, Wea. Forecasting, 31, 1615-1623, doi: https://doi.org/10.1175/WAF-D-16-0053.1, 2016.

Dai, H., Zhao, K., Li, Q., Lee, W. C., Ming, J., Zhou, A., Fan, X., Yang, Z., Zheng, F., and Duan, Y.: Quasi-periodic intensification of convective asymmetries in the outer eyewall of Typhoon Lekima (2019), Geophys. Res. Lett., preprint, doi: 10.1029/2020GL091633, 16 February 2021.

Didlake, A. C., Reasor, P. D., Rogers, R. F., and Lee, W. C.: Dynamics of the transition from Spiral Rainbands to a secondary eyewall in Hurricane Earl (2010), J. Atmos. Sci., 75, 2909-2929, doi: https://doi.org/10.1175/JAS-D-17-0348.1, 2018.

Dudhia, J.: Numerical study of convection observed during the Winter Monsoon Experiment using a mesoscale two dimensional model, J. Atmos. Sci., 46, 3077-3107, doi: https://doi.org/10.1175/1520-0469(1989)046<3077:NSOCOD>2.0.CO;2, 1989.

Emanuel, K. A.: An air-sea interaction theory for tropical cyclones. Part I: Steady-state maintenance, J. Atmos. Sci., 43, 585-605, doi: https://doi.org/10.1175/1520-0469(1986)043<0585:AASITF>2.0.CO;2, 1986.

Fortner, L. E.: Typhoon Sarah, 1956, Bull. Amer. Meteor. Soc., 39, 633-639, doi: https://doi.org/10.1175/1520-0477-39.12.633, 1958.

Hawkins, J. D. and Helveston, M.: Tropical cyclone multiple eyewall characteristics. 28th Conference on Hurricanes and Tropical Meteorology, Orlando, FL, Amer. Meteor. Soc., 14B.1. [Available online at https://ams.confex.com/ams/28Hurricanes/techprogram/paper_138300.htm.], 2008.

Houze, R. A., Jr., Chen, S. S., Smull, B. F., Lee, W. C., and Bell, M. M.: Hurricane intensity and eyewall replacement, Science, 315, 1235-1239, doi: 10.1126/science.1135650, 2007.

Huang, Y. H., Montgomery, M. T., and Wu, C. C.: Concentric eyewall formation in typhoon Sinlaku (2008). PartⅡ: Axisymmetric dynamical processes, J. Atmos. Sci., 69, 662-674, doi: https://doi.org/10.1175/JAS-D-11-0114.1, 2012.

Kain, J. S. and Fritsch, J. M.: Convective parameterization for mesoscale models: The Kain–Fritch scheme. The Representation of Cumulus Convection in Numerical Models, Meteor. Monogr., No. 46, Amer. Meteor. Soc., 165-170, doi: 10.1007/978-1-935704-13-3_16, 1993.

Kepert, J.: How does the boundary layer contribution to eyewall replacement cycles in axisymmetric tropical cyclones? J. Atmos. Sci., 70, 2808-2830, doi: https://doi.org/10.1175/JAS-D-13-046.1, 2013.

Kossin, J. P. and Sitkowski, M.: An objective model for identifying secondary eyewall formation in hurricanes, Mon. Wea. Rev., 137, 876-892, doi: https://doi.org/10.1175/2008MWR2701.1, 2009.

Kuo, H.-C., Lin, L.-Y., Chang, C.-P., and Williams, R. T.: The formation of concentric vorticity structures in typhoons, J. Atmos. Sci., 61, 2722-2734, doi: https://doi.org/10.1175/JAS3286.1, 2004.

——, Schubert, W. H., Tsai, C.-L., and Kuo, Y.-F.: Vortex interactions and the barotropic aspects of concentric eyewall formation, Mon. Weather Rev., 136, 5183-5198, doi: https://doi.org/10.1175/2008MWR2378.1, 2008.

Miller, W., Chen, H., and Zhang, D.-L.: On the rapid intensification of Hurricane Wilma (2005). Part III: Effects of latent heat of fusion, J. Atmos. Sci., 72, 3829-3849, doi: https://doi.org/10.1175/JAS-D-14-0386.1, 2015.

Mlawer, E. J., Taubman, S. J., Brown, P. D., Iacono, M. J., and Clough, S. A.: Radiative transfer for inhomogeneous atmosphere: RRTM, a validated correlated-k model for the longwave, J. Geophys. Res., 102, 16663-16682, doi: https://doi.org/10.1029/97JD00237, 1997.

Montgomery, M. T. and Kallenbach, R. J.: A theory for vortex Rossby-waves and its application to spiral bands and intensity changes in hurricanes, Q. J. R. Meteorol. Soc., 123, 435-465, doi: https://doi.org/10.1002/qj.49712353810, 1997.

Noh, Y., Cheon, W. G., Hong, S.-Y., and Raasch, S.: Improvement of the K-profile model for the planetary boundary layer based on large-eddy simulation data, Bound.-Layer Meteor., 107, 401-427, doi: 10.1023/A:1022146015946, 2003.

Qin N. and Zhang, D.-L.: On the extraordinary intensification of Hurricane Patricia (2015). Part I: Numerical experiments, Wea. Forecasting, 33, 1205-1224, doi: https://doi.org/10.1175/WAF-D-18-0045.1, 2018.

Qin N., Wu, L., and Liu, Q.: Evolution of the moat associated with the secondary eyewall formation in a simulated tropical cyclone, J. Atmos. Sci., under review, 2021.

Qiu X., Tan, Z. M., and Xiao, Q.: The roles of vortex Rossby waves in hurricane secondary eyewall formation, Mon. Wea. Rev., 138, 2092-2109, doi: https://doi.org/10.1175/2010MWR3161.1, 2010.

Qiu X. and Tan, Z. M.: The roles of asymmetric inflow forcing induced by outer rainbands in tropical cyclone secondary eyewall formation, J. Atmos. Sci., 70, 953-974, doi: https://doi.org/10.1175/JAS-D-12-084.1, 2013.

Rozoff, C. M., Nolan, D. S., Kossin, J. P., Zhang, F., and Fang, J.: The roles of an expanding wind field and inertial stability in tropical cyclone secondary eyewall formation, J. Atmos. Sci., 69, 2621-2643, doi: https://doi.org/10.1175/JAS-D-11-0326.1, 2012.

Samsury C. E. and Zipser, E. J.: Secondary wind maxima in hurricanes: Airflow and relationship to rainbands, Mon. Wea. Rev., 123, 3502-3517, doi: https://doi.org/10.1175/1520-0493(1995)123<3502:SWMIHA>2.0.CO;2, 1995.

Smith, R. K., Montgomery, M. T., and Zhu, H.: Buoyancy in tropical cyclones and other rapidly rotating vortices, Dyn. Atmos. Oceans, 40, 189-208, doi:10.1016/j.dynatmoce.2005.03.003, 2005.

Sun Y. Q., Jiang, Y. X., Tan, B. K., and Zhang, F.: The governing dynamics of the secondary eyewall formation of typhoon Sinlaku (2008), J. Atmos. Sci., 70, 3818-3837, doi: https://doi.org/10.1175/JAS-D-13-044.1, 2013.

Terwey, W. D. and Montgomery, M. T.: Secondary eyewall formation in two idealized, full-physics modeled hurricanes, J. Geophys. Res. Atmos., 113, 1-18, doi: https://doi.org/10.1029/2007JD008897, 2008.

Tyner, B., Zhu, P., Zhang, J. A., Gopalakrishnan, S., Marks, F., and Tallapragada, V.: A top-down pathway to secondary eyewall formation in simulated tropical cyclones, J. Geophys. Res. Atmos., 123, 174-197, doi: https://doi.org/10.1002/2017JD027410, 2018.

Wang, Y.: An explicit simulation of tropical cyclones with a triply nested movable mesh primitive equation model: TCM3. Part II: Model refinements and sensitivity to cloud microphysics parameterization, Mon. Wea. Rev., 130, 3022-3036, doi: https://doi.org/10.1175/1520-0493(2002)130<3022:AESOTC>2.0.CO;2, 2002.

Wang, Y.: How do outer spiral rainbands affect tropical cyclone structure and intensity? J. Atmos. Sci., 66, 1250-1273, doi: https://doi.org/10.1175/2008JAS2737.1, 2009.

Wang, H., Wang, Y., Xu, J., and Duan, Y.: The axisymmetric and asymmetric aspects of the secondary eyewall formation in numerically simulated tropical cyclone under idealized conditions on an *f* plane, J. Atmos. Sci., 76, 357-378, doi: https://doi.org/10.1175/JAS-D-18-0130.1, 2019.

Wang, Y-F and Tan, Z-M.: Outer rainbands–driven secondary eyewall formation of tropical cyclones, J. Atmos. Sci., 77, 2217-2236, doi: https://doi.org/10.1175/JAS-D-19-0304.1, 2020.

Willoughby, H. E., Clos, J. A., and Shoreibah, M. G.: Concentric eye walls, secondary wind maxima, and the evolution of the hurricane vortex, J. Atmos. Sci. 39, 395-411, doi: https://doi.org/10.1175/1520-0469(1982)039<0395:CEWSWM>2.0.CO;2, 1982.

Wu, L., Liu, Q., and Li, Y.: Prevalence of tornado-scale vortices in the tropical cyclone eyewall, P. Natl. Acad. Sci., 115, 8307- 8310, doi: https://doi.org/10.1073/pnas.1807217115, 2018.

Wu, L., Liu, Q., and Li, Y.: Tornado-scale vortices in the tropical cyclone boundary layer: numerical simulation with the WRF–LES framework, Atmos. Chem. Phys., 19, 2477-2487, doi: https://doi.org/10.5194/acp-19-2477-2019, 2019.

Wunsch, K. E. D. and Didlake, A. C.: Analyzing tropical cyclone structures during secondary eyewall formation using aircraft in situ observations, Mon. Wea. Rev., 146, 3977-3993, doi: https://doi.org/10.1175/MWR-D-18-0197.1, 2018.

Yau, M. K., Liu, Y., Zhang, D.-L., and Chen, Y.: A multiscale numerical study of Hurricane Andrew (1992). Part VI: Small-scale inner-core structures and wind streaks, Mon. Wea. Rev., 132, 1410-1433, doi: https://doi.org/10.1175/1520-0493(2004)132<1410:AMNSOH>2.0.CO;2, 2004.

Yu, C.-L., Didlake, A. C. Jr., Zhang, F., and Nystrom, R. G.: Asymmetric rainband processes leading to secondary eyewall formation in a model simulation of Hurricane Matthew (2016), J. Atmos. Sci., 78, 29-49, doi: https://doi.org/10.1175/JAS-D-20-0061.1, 2020.

Zhang, D.-L., Liu, Y., and Yau, M. K.: A multiscale numerical study of Hurricane Andrew (1992). Part III: Dynamically induced vertical motion, Mon. Wea. Rev., 128, 3772-3788, doi: https://doi.org/10.1175/1520-0493(2001)129<3772:AMNSOH>2.0.CO;2, 2000.

Zhang, D.-L., Lin, Z., Zhang, X., and Tallapragada, V.: Sensitivity of idealized hurricane intensity and structures under varying background flows and initial vortex intensities to different vertical resolutions in HWRF, Mon. Wea. Rev., 143, 914-932, doi: https://doi.org/10.1175/MWR-D-14-00102.1, 2015.

Zhao, K., Lee, W.-C., and Jou, B. J.-D.: Single Doppler radar observation of the concentric eyewall in Typhoon Saomai, 2006, near landfall. Geophys. Res. Lett., 35, L07807, doi: https://doi.org/10.1029/2007GL032773, 2008.

Zhao, K., Lin, Q., Lee, W-C., Sun, Y., and Zhang, F.: Doppler radar analysis of triple eyewalls in Typhoon Usagi (2013). Bull. Amer. Meteor. Soc., 97, 25-30, doi: https://doi.org/10.1175/BAMS-D-15-00029.1, 2016.

Zhu, T., and Zhang, D.-L.: Numerical simulation of Hurricane Bonnie (1998). Part II: Sensitivity to varying cloud microphysical processes, J. Atmos. Sci., 63, 109-126, doi: https://doi.org/10.1175/JAS3599.1, 2006.

Zhu, Z., and Zhu, P.: The role of outer rainband convection in governing the eyewall replacement cycle in numerical simulations of tropical cyclones, J. Geophys. Res. Atmos., 119, 8049-8072, doi: 10.1002/2014JD021899, 2014.

Zhu Z., and Zhu, P.: Sensitivities of eyewall replacement cycle to model physics, vortex structure, and background winds in numerical simulations of tropical cyclones, J. Geophys. Res. Atmos., 120, 590-622, doi: 10.1002/2014JD022056, 2015.

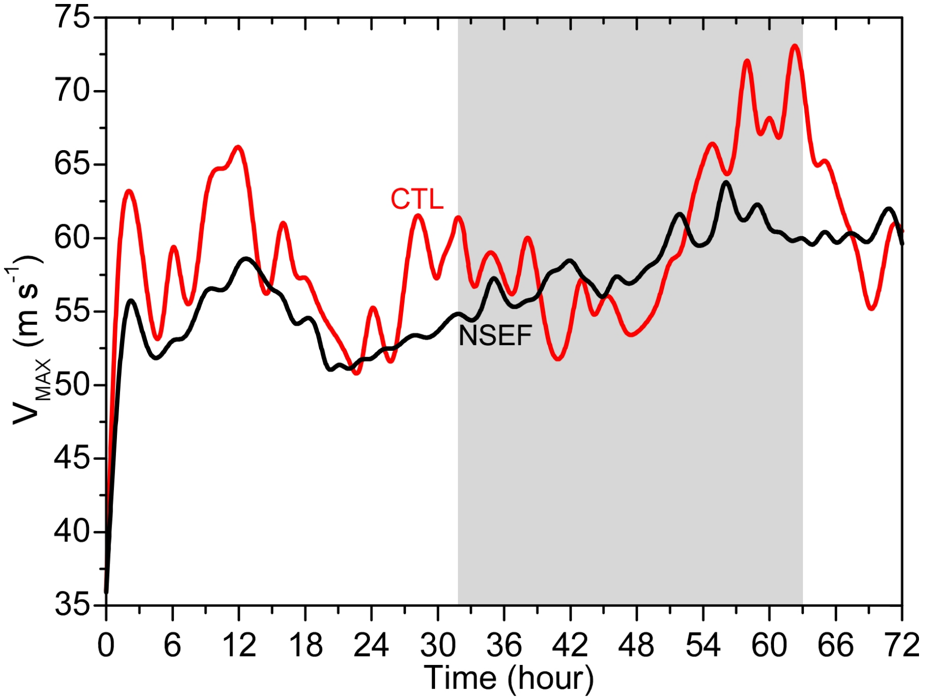

Figure 1. Time series of intensity changes for the maximum azimuthal-mean near-surface wind (V_{MAX}, m s^{-1}) during the 72-h sensitivity (NSEF, black) and control run (CTL, red). The gray shading denotes the period of the eyewall replacement circle.

https://doi.org/10.5194/acp-2021-147
Preprint. Discussion started: 7 April 2021

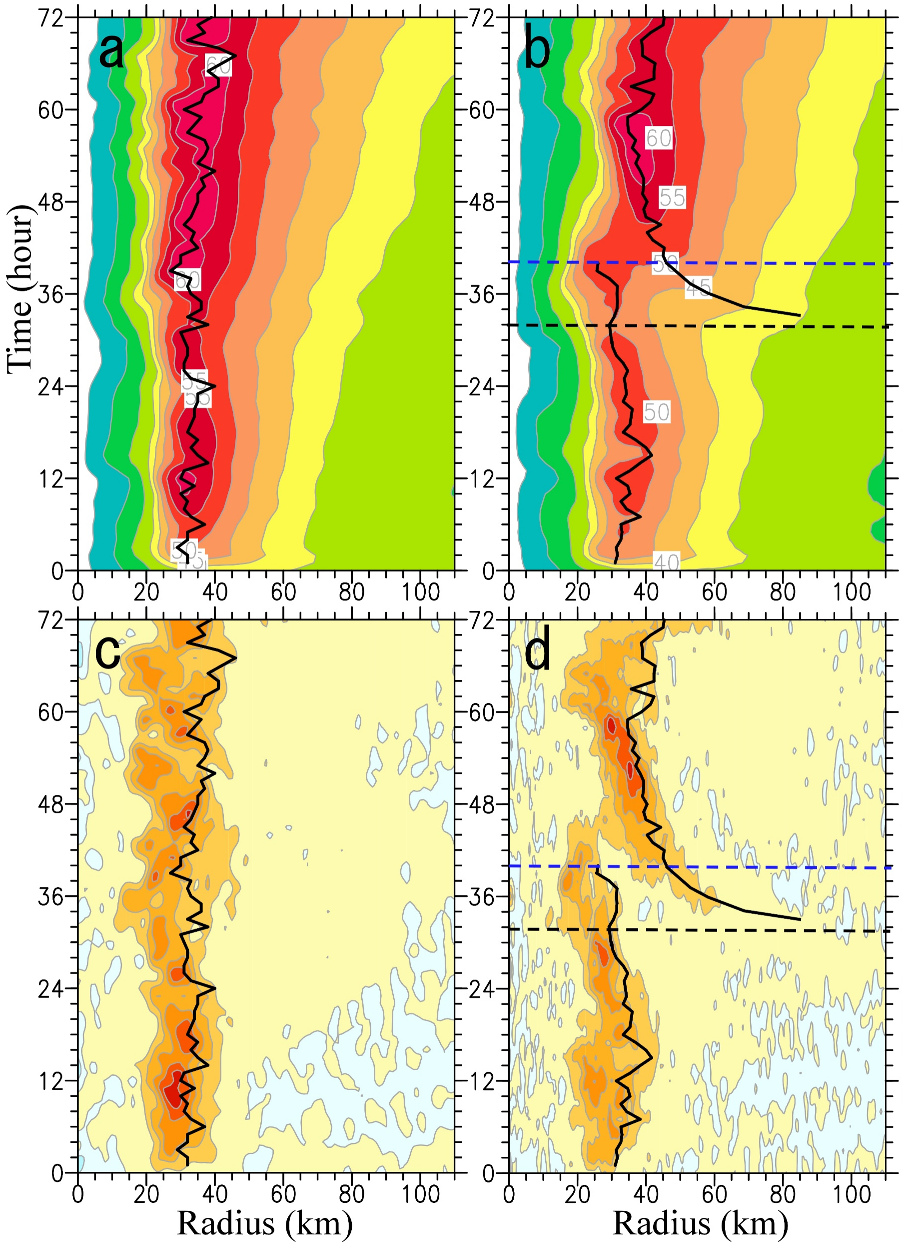

Figure 2. Time-radius cross-sections of the azimuthal-mean (a, b) tangential wind (m s^{-1}) and (c, d) vertical motion (m s^{-1}) at 0.5-km height for (a, c) NSEF and (b, d) CTL. The solid lines indicate the radius of the maximum tangential wind (RMW). The black dashed lines indicate the SEF, while the blue dashed lines denote the time when the secondary maximum wind is equal to the primary maximum wind.

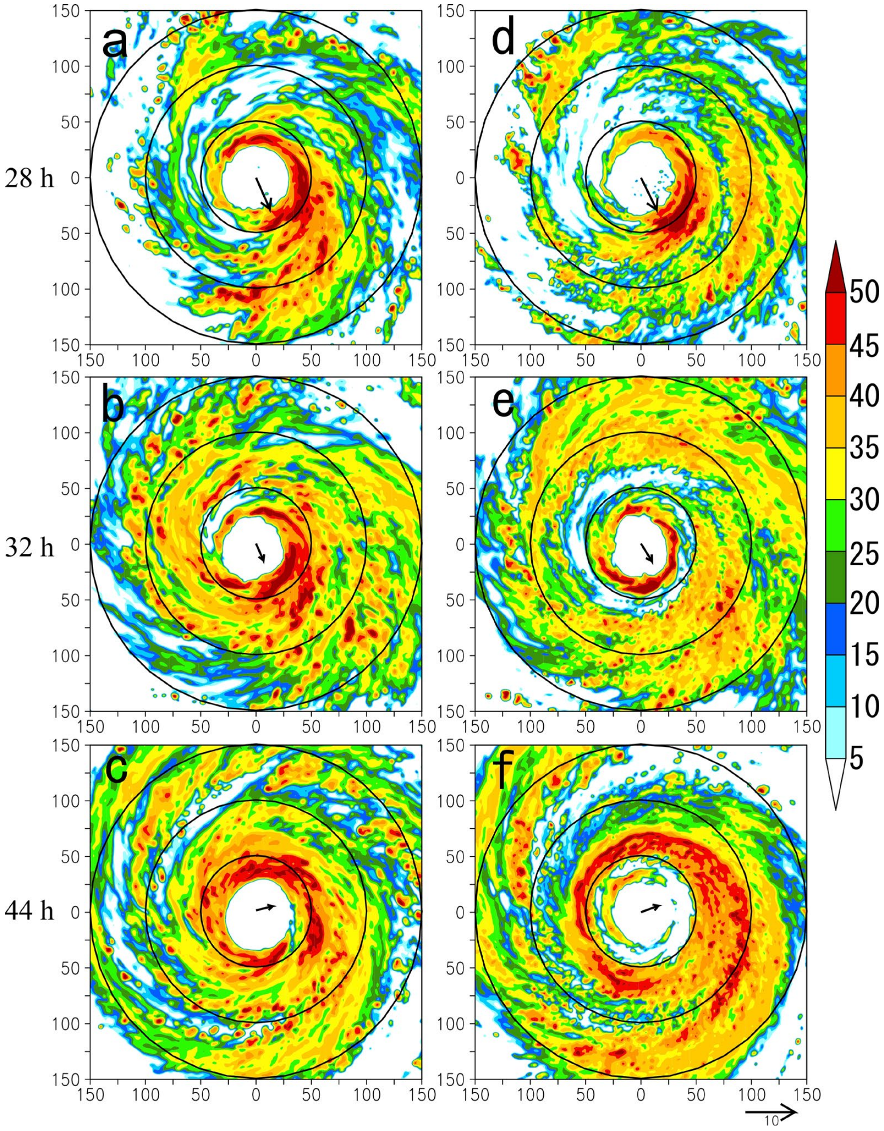

Figure 3. Horizontal distributions of the radar reflectivity at 5-km height at (a, d) 28, (b, e) 32, and (c, f) 44 h for (a-c) NSEF and (d-f) CTL. Vectors are the large-scale vertical wind shear (VWS, Vspeed (200 hPa) -Vspeed (850 hPa)).

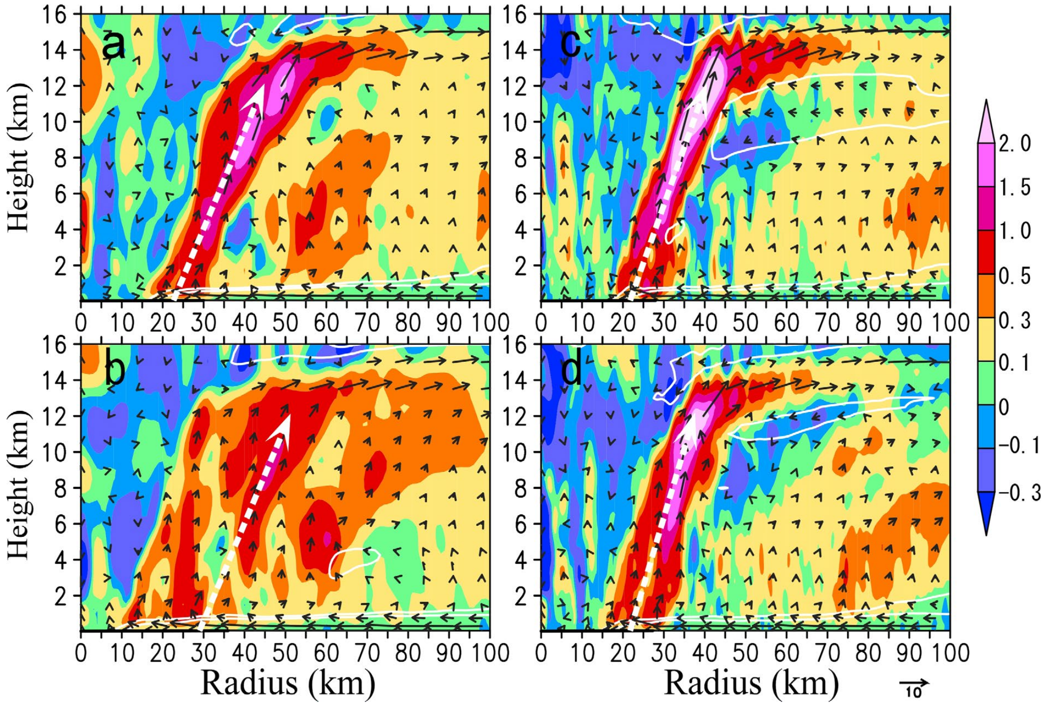

Figure 4. Radius-height cross-sections of the azimuthal-mean vertical motion (shaded, m s^{-1}), in-plain flow (vector, m s^{-1}) and radial inflows of -1 and -3 m s^{-1} (white contours) at (a, c) 30 h and (b, d) 32 h for (a, b) NSEF and (c, d) CTL. The white dashed arrows denote the eyewall.

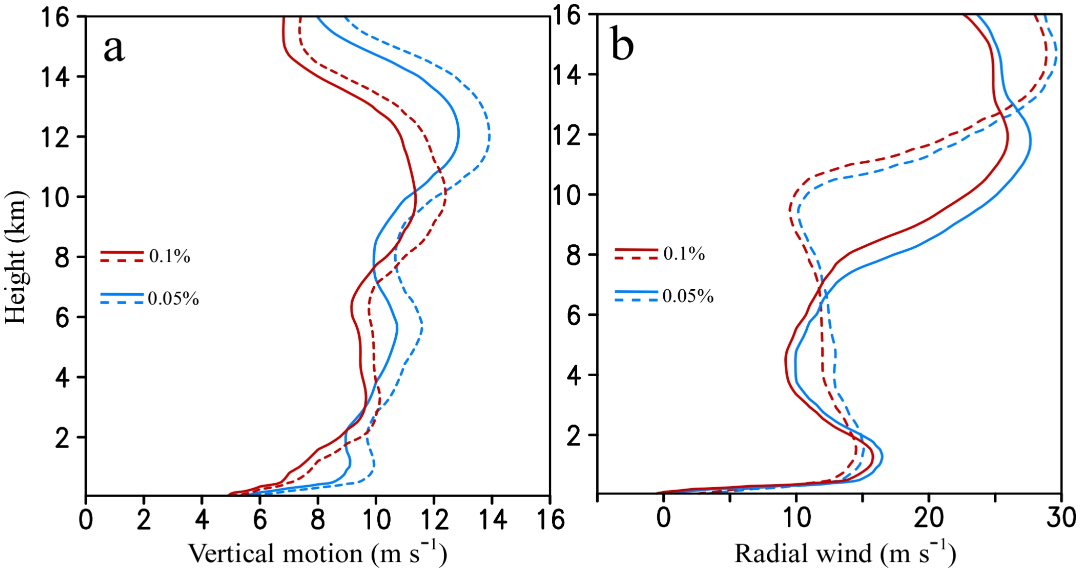

Figure 5. The contoured frequency by altitude diagram (CFAD, %) of (a) the vertical motion for the 10-km radially inside and outside of the RMW and (b) the radial wind within a radial distance of 60 km starting from the radius of 10-km outside the eyewall (RMW+10 km to RMW+70 km) for CTL (dashed lines) and NSEF (solid lines) at 30 h. The red and blue lines are the 0.1, and 0.05 percentile.

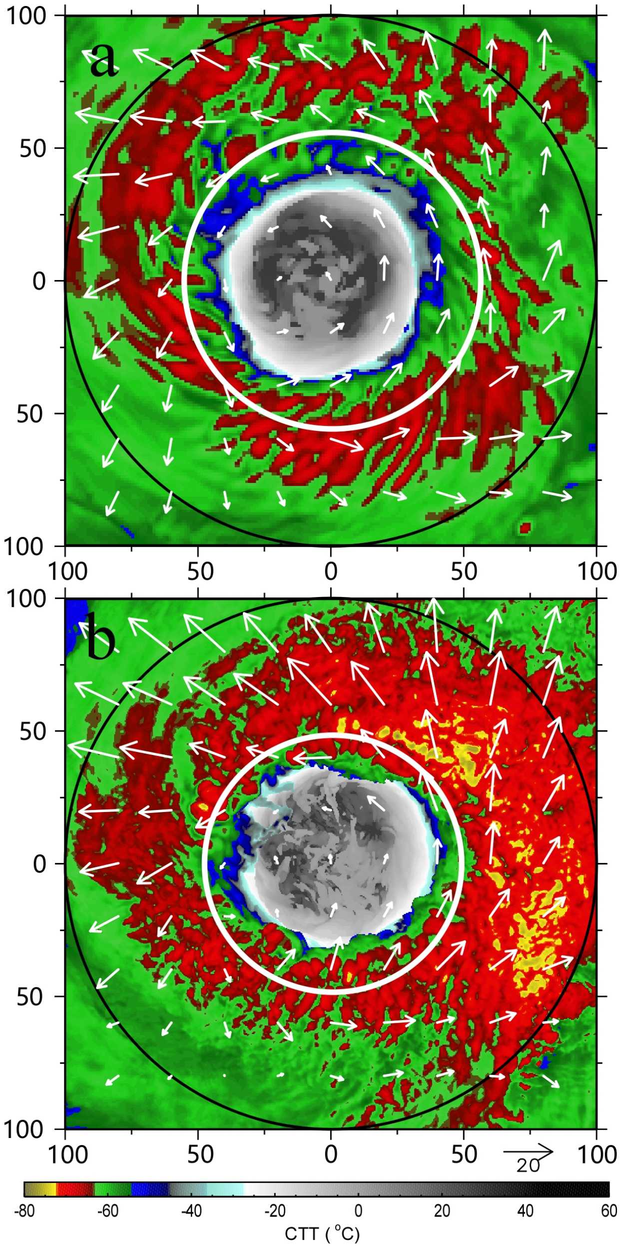

Figure 6. Horizontal distribution of the cloud-top temperature (CTT, shaded, C°) superimposed with the 15-km horizontal wind field (vector, m s^{-1}) and RMW (white circle) at 30 h for (a) NSEF and (b) CTL. The black circle indicates the radius of 100 km relative to the TC center.

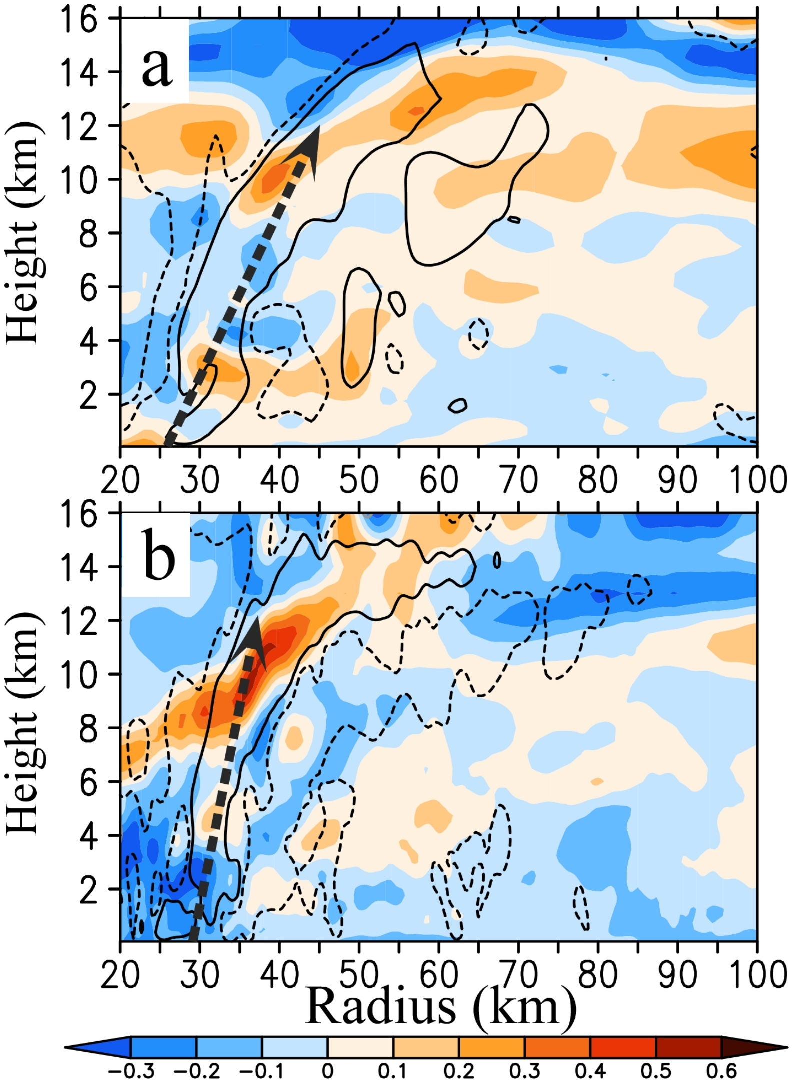

Figure 7. Radius-height cross-sections of the upshear-right quadrant-mean perturbation virtual potential temperature (shaded, K) at 30 h for (a) NSEF and (b) CTL. Contours are the vertical motion (updraft, black solid contours: 0.5 m s^{-1}; downdrafts, black dashed contours: 0.05 m s^{-1}). The black dashed arrows denote the eyewall.

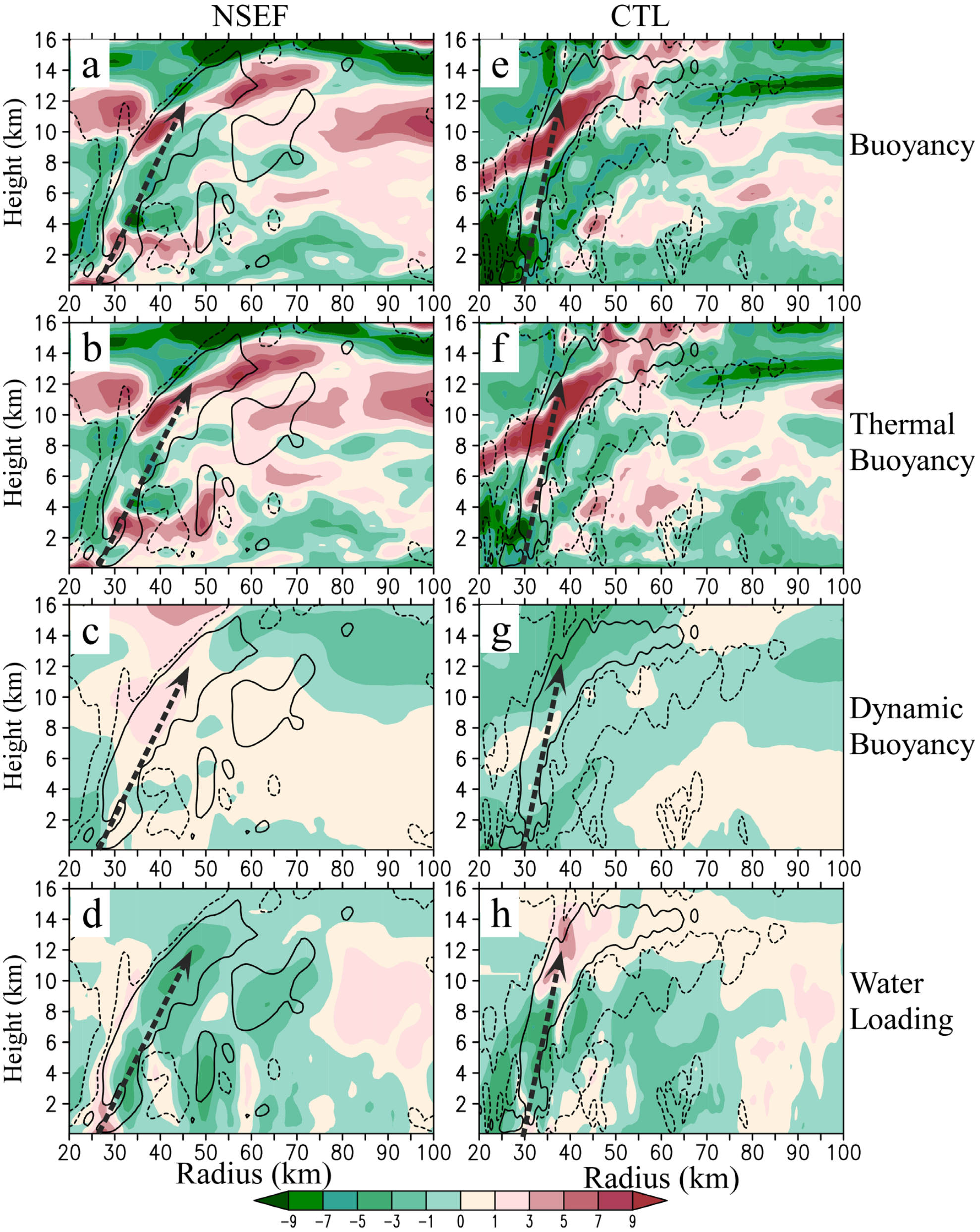

Figure 8. Radius-height cross-sections of the upshear-right quadrant-mean (a, e) buoyance force (shaded, 10^{-3} m s^{-2}), (b, f) the thermal buoyancy (shaded, 10^{-3} m s^{-2}), (c, g) the dynamic buoyancy (shaded, 10^{-3} m s^{-2}), and (d, h) the hydrometeor loading (shaded, 10^{-3} m s^{-2}) superimposed with the vertical motion (updraft, black solid contours: 0.5 m s^{-1}; downdrafts, black dashed contours: 0.05 m s^{-1}) at 30 h for (a-d) NSEF and (e-h) CTL. The black dashed arrows denote the eyewall.

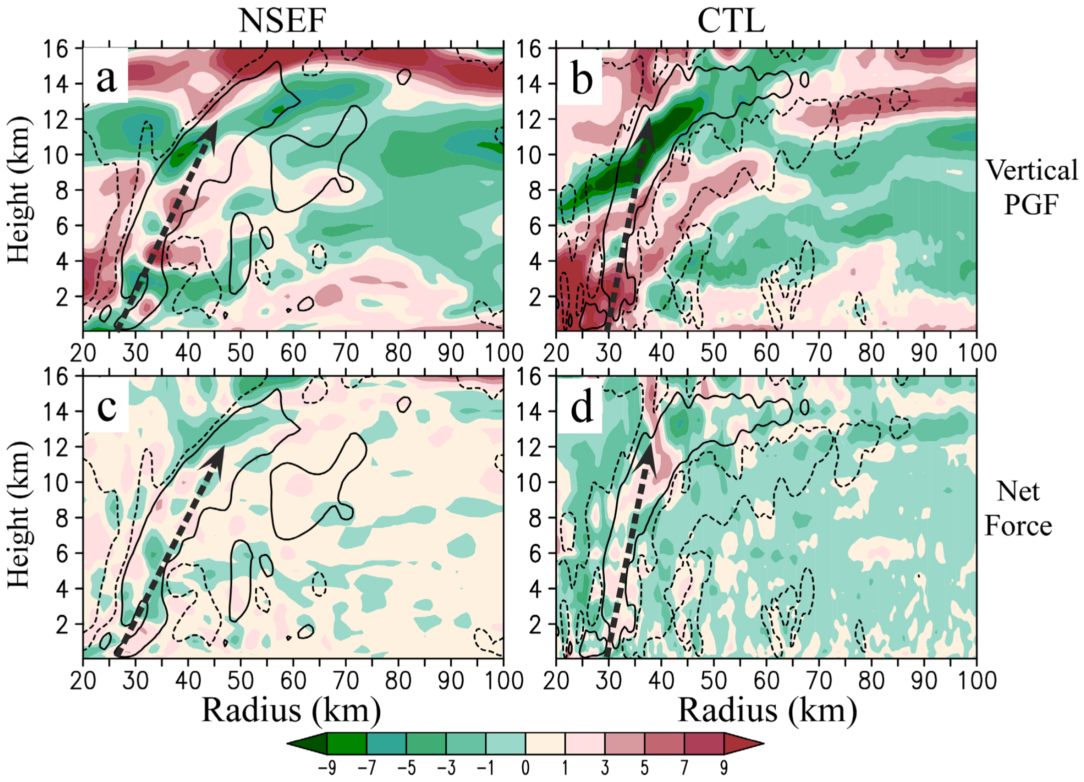

Figure 9. Radius-height cross-sections of the upshear-right quadrant-mean (a, b) vertical pressure gradient force (shaded, 10^{-3} m s^{-2}) and (c, d) the sum of buoyancy and vertical pressure gradient force (shaded, 10^{-3} m s^{-2}), superimposed with the vertical motion (updraft, black solid contours: 0.5 m s^{-1}; downdrafts, black dashed contours: 0.05 m s^{-1}) at 30 h for (a, c) NSEF and (b, d) CTL. The black dashed arrows denote the eyewall.

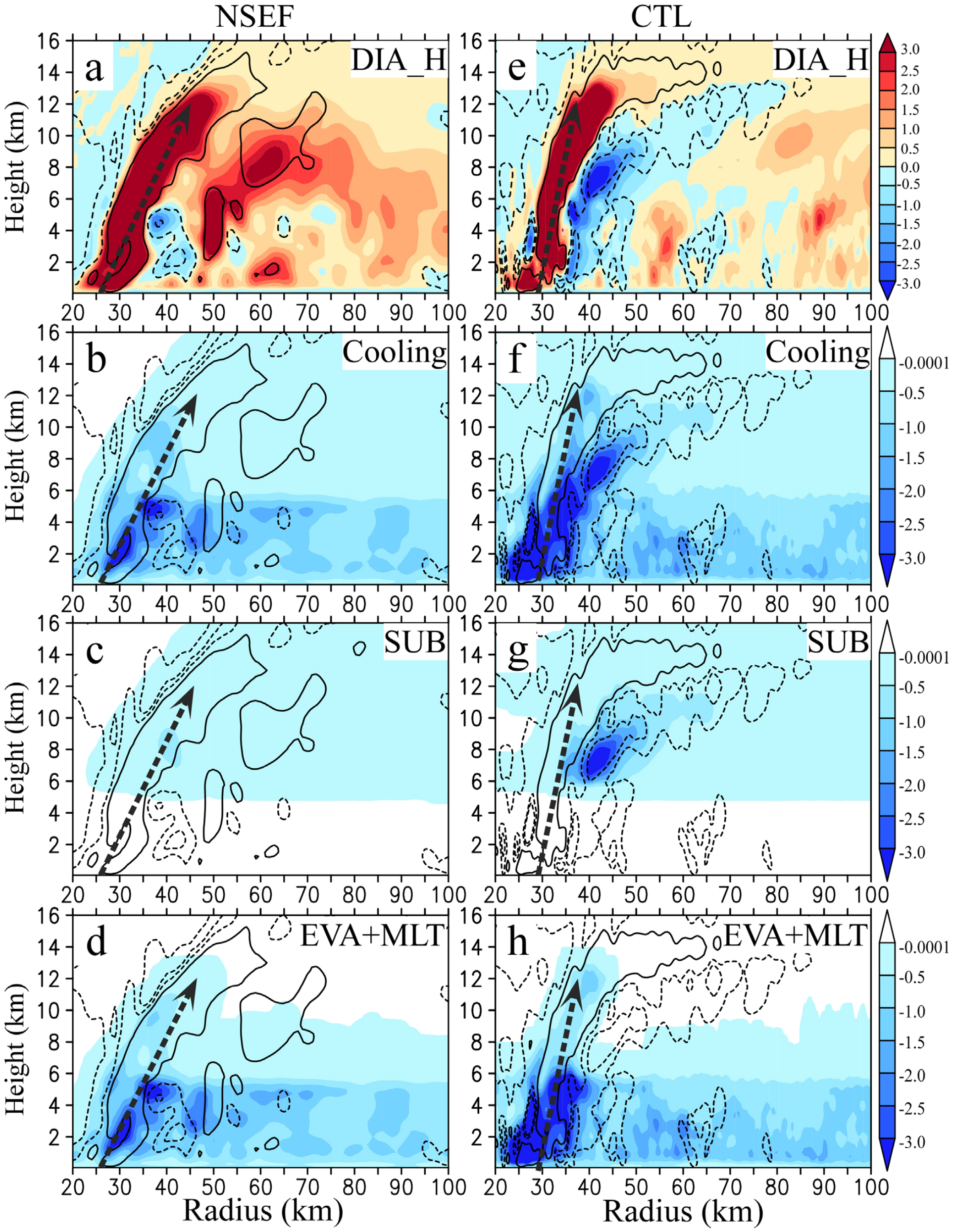

Figure 10. Radius-height cross-sections of the upshear-right quadrant-mean (a, e) diabatic heating rate (shaded, 10^{-3} K s^{-1}), (b, f) cooling rate including evaporation, melting and sublimation processes (shaded, 10^{-3} K s^{-1}), (c, g) sublimation cooling rate, and (d, h) melting and evaporation cooling rates superimposed with the vertical motion (updraft, solid lines of 0.5 m s^{-1}; downdrafts, dashed lines of -0.05 and -0.3 m s^{-1}) at 30 h for (a-d) NSEF and (e-h) CTL. The black dashed arrows denote the eyewall.

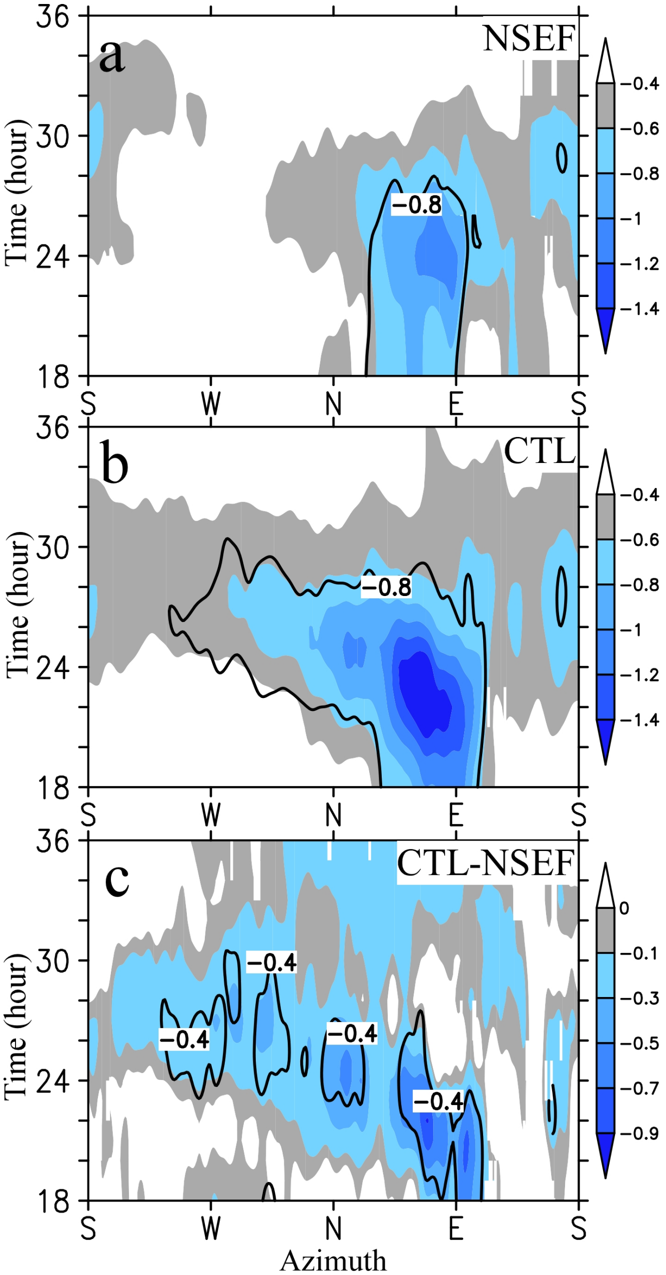

589

590 Figure 11. Azimuthal-time cross-sections of the layer-mean (11.5-12.5 km) diabatic cooling
591 (shaded, 10^{-3} K s^{-1}) and subsidence (contour, m s^{-1}) averaged within a radial distance of 25
592 km starting from the radius of 5-km outside the eyewall (RMW+5 km to RMW+30 km) of
593 (a) NSEF, (b) CTL, and (c) differences between CTL and NSEF. The black contours are -0.8
594 m s^{-1} in (a, b) and -0.4 m s^{-1} in (c).

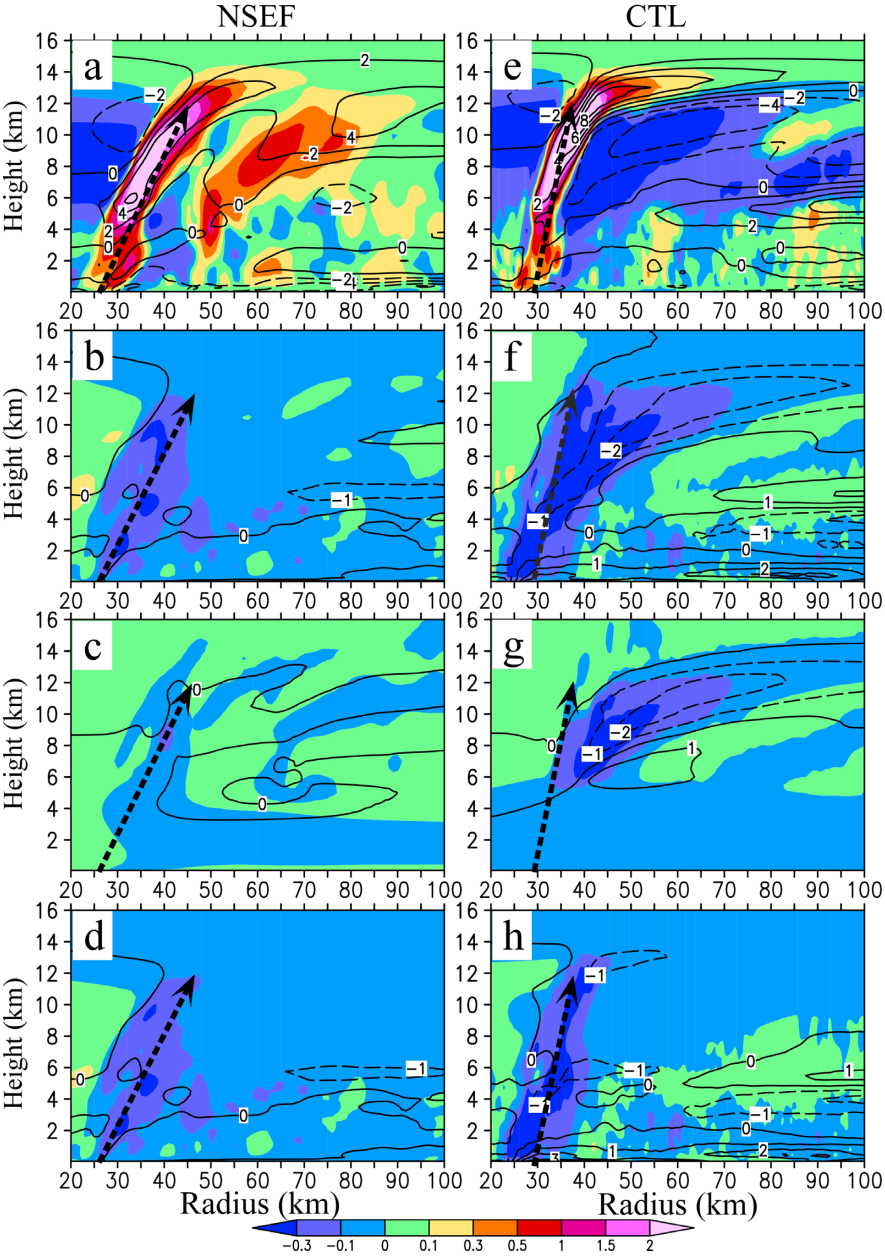

Figure 12. Radius-height cross-sections of the upshear-right quadrant-mean vertical (shaded, m s^{-1}) and radial motion (contours, m s^{-1}) forced by the (a, e) diabatic heating, (b, f) hydrometeors cooling, (c, g) sublimation cooling, (d, h) melting and evaporation cooling at 30 h for (a-d) NSEF and (c-h) CTL. Note that the radial wind is at 2 m s^{-1} intervals in (a) and (e), and 1 m s^{-1} intervals in others. The white dashed lines with 0.5 m s^{-1} vertical motion indicate the eyewall convection region. The black dashed arrows denote the eyewall.

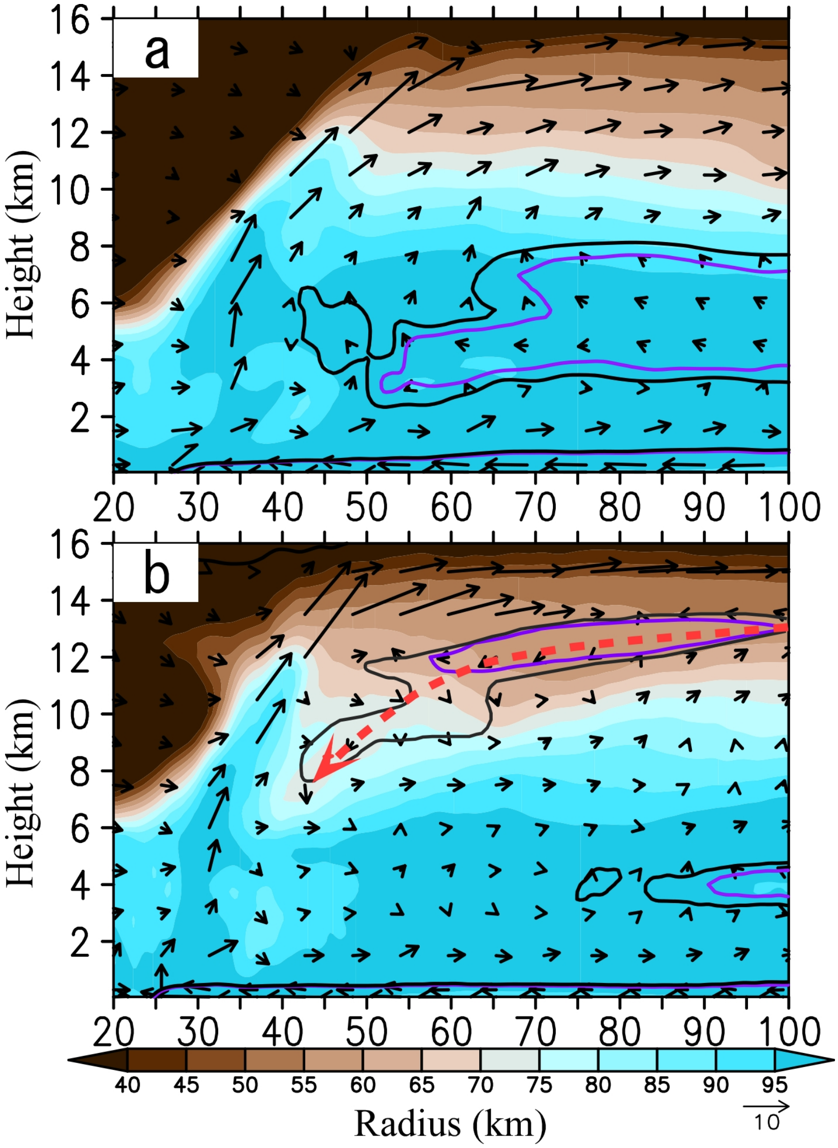

Figure 13. Radius-height cross-sections of the the upshear-right quadrant-mean relative humidity (shaded, %) and in-plain flows (vector, m s^{-1}) at t = 30 h for (a) NSEF and (b) CTL. The black and purple lines are radial inflows of -0.01 and -1 m s^{-1}, respectively. The red dashed arrow indicates the upper-level dry inflows.

https://doi.org/10.5194/acp-2021-147
Preprint. Discussion started: 7 April 2021

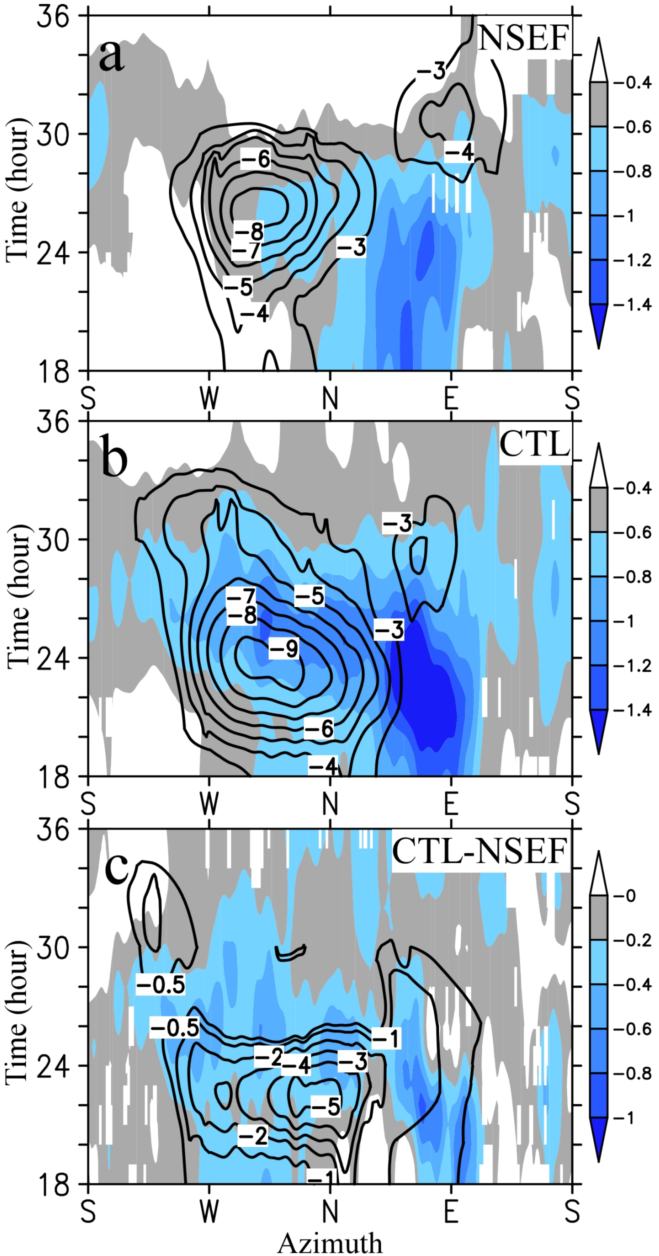

Figure 14. Same as in Fig. 11 but for subsidence (shaded, m s^{-1}) and radial inflows (contour, m s^{-1}) of (a) NSEF, (b) CTL, and (c) differences between CTL and NSEF.

https://doi.org/10.5194/acp-2021-147
Preprint. Discussion started: 7 April 2021

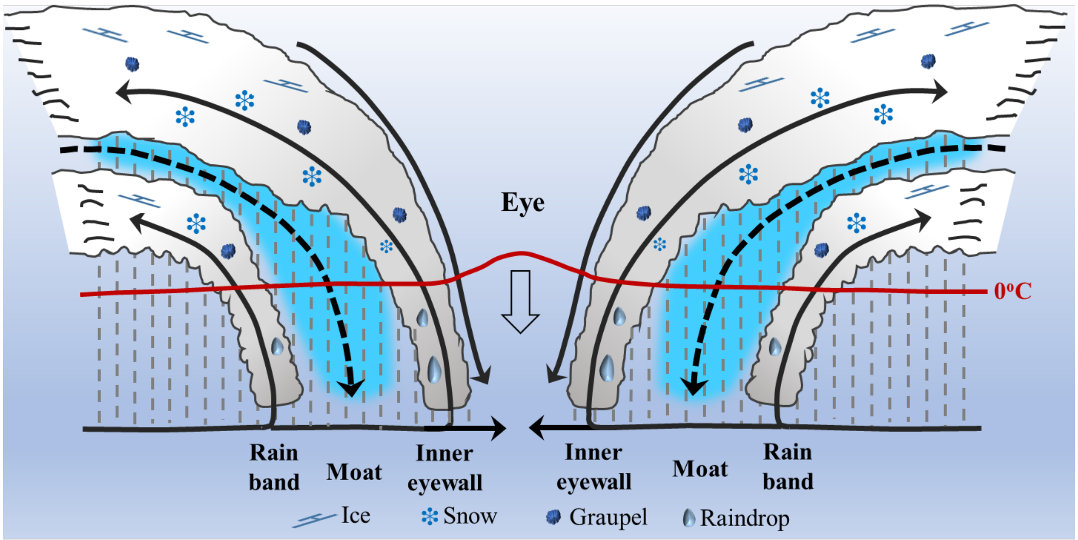

Figure 15. The inner-core structures of a hurricane undergoing the eyewall replacement circle, including the eye, the primary eyewall, the moat, and the rainband of evolving into the secondary eyewall. The black solid arrows denote the air motion relative to the TC. The black dashed arrows show the upper-level descending inflows beneath the cumulus anvil from the inner eyewall. The light blue shading indicates the cooling induced by the sublimation, melting, and evaporation of hydrometeors (ice, snow, graupel, and raindrops) associated with the moat subsidence. The gray dashed lines indicate the precipitation below the clouds. The red solid line denotes the 0 °C temperature of the melting level.